Contributions of inner-valence molecular orbitals and multiphoton resonances to high-order-harmonic generation of N_2: A time-dependent density-functional-theory study

Xi Chu
Department of Chemistry and Biochemistry, The University of Montana, Missoula, Montana 59812, USA

Gerrit C. Groenenboom
Institute for Molecules and Materials, Radboud University Nijmegen, Heyendaalseweg 135, 6525 AJ Nijmegen, The Netherlands
(Received 14 December 2015; published 25 January 2016)

Using a time-dependent density-functional-theory (TDDFT) method, we calculated the high-harmonic generation (HHG) spectra of N_2 in 800- and 1300-nm intense lasers. The calculations reproduce the experimentally observed minimum near 40 eV and the shift of the minimum due to interference of different molecular orbitals. They also support the proposed shape resonance near 30 eV. The TDDFT method allows us to analyze the involvement of different electronic configurations in the HHG process. We identified a significant role of Rydberg states and autoionizing states in enhancing HHG. This finding is consistent with studies of photoelectron spectra in a similar energy range. Moreover, we discover a significant contribution of the $2\sigma_g$ orbital above 40 eV, demonstrating the complexity of electronic structure information contained in molecular HHG. At high energy not only the HOMO and HOMO-1 are important, as suggested by earlier studies, but the HOMO-3 contributes substantially as well.

DOI: 10.1103/PhysRevA.93.013422

I. INTRODUCTION

High-harmonic generation (HHG) has given rise to remarkable progress in attosecond chemistry and N_2 is one of the most extensively studied molecules. The HHG of N_2 has enabled imaging of molecular orbitals [1,2] and monitoring ultrafast nuclear dynamics [3]. For N_2 the Cooper minimum [4–6] and resonances [6,7] in HHG and the relationship between HHG and photoelectron spectroscopy [8] are under investigation for future applications.

A widely accepted three-step model [9,10] describes HHG as follows: (i) the molecule in the gas phase ionizes through tunneling; (ii) the free electron quivers in the field; and (iii) it recollides with the parent ion and emits high-harmonic photons. The most commonly adopted approach to calculate HHG is described by Lewenstein *et al.* [11]. It is based on the strong-field approximation [12–14], which assumes that the interaction between the ionized electron and the parent ion can be neglected and that the initial state is the field free state. It relates HHG to the dipole matrix element for recombination of a free electron with the proper kinetic energy to the highest occupied molecular orbital (HOMO). Involvement of the HOMO-1, however, has attracted substantial attention, which lead to imaging of the $1\pi_u$ HOMO-1 orbital of N_2 [2,4,15].

Experiments use a pump-probe setup to compare HHG yields for parallel and perpendicular orientation of the molecular axis with respect to the laser polarization [8,15]. If a harmonic emission is stronger for the parallel orientation, it is considered to arise from the HOMO and if the signal is more intense for the perpendicular orientation, it is assigned to the HOMO-1 [15]. Such a setup assumes negligible contributions from all other orbitals, although abundant photoelectron spectroscopic data of N_2 have been related to those orbitals [16] and the recombination process of HHG may be considered the reverse of photoionization. In this article we reexamine this assumption using time-dependent density-functional-theory (TDDFT) calculations, which treat all electrons and orbitals.

Recombination is the reverse of photoionization; therefore, HHG and photoionization spectra should be related [7]. The interpretation of measured photoionization cross sections (PICSs) may assist in analyzing features of HHG spectra, such as Cooper minima and shape resonances. Involvement of multiple molecular orbitals, however, complicates the comparison. The PICS is an incoherent sum of partial PICSs, whereas HHG arises from the coherent addition of contributions from molecular orbitals, which causes a notable difference for N_2 in the energy range of 20–26 eV: the $A\,^2\Pi_u$ state (a hole in the HOMO-1) dominates over the $X\,^2\Sigma_g^+$ state (a hole in the HOMO) in partial PICSs [17] but the other way around in angle resolved HHG [8,15,18]. The $A\,^2\Pi_u$ state is 1.3 eV higher in energy than the $X\,^2\Sigma_g^+$ state. This difference between HHG and PICS was explained by an analysis based on TDDFT calculations [6], which showed that a multiphoton resonance between the $3\sigma_g \rightarrow 2\pi_u$ Rydberg state and the $2\sigma_u \rightarrow 1\pi_g$ autoionizing state enhances contributions of the HOMO over those of the HOMO-1 in HHG. This resonance is significant when the angle between the molecular axis and the laser polarization is large, i.e., near the perpendicular orientation, for which contributions of the HOMO-1 to HHG are nearly maximized. When the orientation angle is small, contributions of the HOMO are dominant due to shape resonances.

The main contributions to HHG arise from the transition dipole moment,

$$\boldsymbol{d}(\omega) = A\langle 3\sigma_u|\hat{\boldsymbol{d}}|\varphi_{\boldsymbol{k}}\rangle + B\langle 2\pi_u|\hat{\boldsymbol{d}}|\varphi_{\boldsymbol{k}'}\rangle + C\langle X\,^2\Sigma_g^+|\hat{\boldsymbol{d}}|C\,^2\Sigma_u^+\rangle + D\langle X\,^2\Sigma_g^+|\hat{\boldsymbol{d}}|2\,^2\Pi_u\rangle + \cdots, \quad (1)$$

where ω is between 20 and 36 eV, $\varphi_{\boldsymbol{k}}$ and $\varphi_{\boldsymbol{k}'}$ are free electron wave functions with proper energies, and A, B, C, D, are coefficients that depend on ω and on the orientation of the molecule relative to the field. The first two terms describe recombination of the free electron, which initially occupies the HOMO, to a Rydberg orbital. Around 40 eV, the two

 ©2016 American Physical Society

terms are minimized, which leads to a Cooper minimum [6]. The third and fourth terms are the induced dipole of the ion. The $\langle X\,^2\Sigma_g^+|\hat{\boldsymbol{d}}|C\,^2\Sigma_u^+\rangle$ matrix element is dominantly a dipole transition from the $1\pi_u$ to the $1\pi_g$ orbital and hence considered as a contribution of the HOMO-1. The $A\langle 3\sigma_u|\hat{\boldsymbol{d}}|\varphi_{\boldsymbol{k}}\rangle$ and $C\langle X\,^2\Sigma_g^+|\hat{\boldsymbol{d}}|C\,^2\Sigma_u^+\rangle$ terms are only significant when the orientation angle is small. They arise from a shape resonance that involves the $3\sigma_g \rightarrow 3\sigma_u$ Rydberg state and the $1\pi_u \rightarrow 1\pi_g$ autoionizing state, which is consistent with the observed PICS [17].

The shape resonance at 30 eV was studied by angle resolved HHG [8] and quantitative rescattering (QRS) theory [7], which expresses the induced dipole moment as a product of the transition dipole determined through electronic structure calculations and a factor using a reference system. Effects such as coupling between the Rydberg and autoionizing states, however, are not included in QRS.

In our TDDFT method the initial state is represented by a single determinant, the time-dependent electronic state, however, evolves into a multiconfigurational state. As such, effects caused by the involvement of multiple ionic states and the interference between different channels are all included. The method utilizes a spacial grid, typically of 120–300 a_0 (bohr) radius, to allow creation of a free electron and an absorbing boundary starting at 40–80 a_0 to simulate ionization. Hence, this method includes multiple electronically excited states, the depletion of the ground state, and the interaction between the active electron and the parent ion in the continuum. On one hand, ionization and HHG are competing processes. On the other hand, different orientation preference between the HOMO and HOMO-1 in terms of ionization is believed to be the cause of the orientation dependence of the contributions of the HOMO and HOMO-1 to HHG. Treating them simultaneously thus improves the accuracy of the HHG calculation. Our TDDFT method has reproduced the full CI results of the ionization of H_2 [19], the measured isotope effects of HHG of H_2 [20], and the measured ionization rates for N_2 and F_2 as a function of laser intensity [21].

We now extend the earlier TDDFT study of HHG in N_2 to cases where the cutoff is beyond 60 eV to explore the possible involvement of inner valence orbitals. The cases involve incident lasers of 800 and 1300 nm, with which measurements have been made [5,7,8].

II. TIME-DEPENDENT DENSITY-FUNCTIONAL THEORY FOR MOLECULES IN INTENSE LASERS

The TDDFT formalism that describes homonuclear diatomic molecules in intense laser fields can be found in the literature [6,22,23]. Here, we give a brief account, adopting atomic units.

The electron density at the position of the electron $\boldsymbol{r}$ and time t is

$$\rho(\boldsymbol{r},t) = \sum_\sigma \sum_{i=1}^{N_\sigma} \rho_{i\sigma}(\boldsymbol{r},t) = \sum_\sigma \sum_{i=1}^{N_\sigma} \psi_{i\sigma}^*(\boldsymbol{r},t)\psi_{i\sigma}(\boldsymbol{r},t), \quad (2)$$

where i is the orbital index, σ is the spin index, and the spin orbital $\psi_{i\sigma}(\boldsymbol{r},t)$ is obtained by solving the time-dependent equations

$$\begin{aligned} i\frac{\partial}{\partial t}\psi_{i\sigma} &= \hat{H}(\boldsymbol{r},t;R)\psi_{i\sigma} \\ &= \left[-\frac{1}{2}\nabla^2 + v_{\rm nucl}(\boldsymbol{r};R) + \boldsymbol{E}(t)\cdot\boldsymbol{r} \right. \\ &\quad \left. + \iiint d^3\boldsymbol{r}'\frac{\rho(\boldsymbol{r}',t;R)}{|\boldsymbol{r}-\boldsymbol{r}'|} + V_{{\rm LB}_\alpha,\sigma}(\boldsymbol{r},t;R)\right]\psi_{i\sigma}, \\ &\quad i = 1,2,\ldots,N_\sigma, \end{aligned} \quad (3)$$

where N_σ is the number of electrons that have σ spin, $\boldsymbol{E}(t) = E(t)\hat{\boldsymbol{q}}$ is the electric field of the laser, $|\hat{\boldsymbol{q}}|=1$, and $v_{\rm nucl}$ is the nuclear attraction.

We employ the LB_α exchange-correlation functional, whose accuracy in strong-field calculations has been benchmarked extensively [19,22–24]. The time-dependent LB_α potential is

$$\begin{aligned} &V_{{\rm LB}_\alpha,\sigma} \\ &= \alpha v_{x\sigma}^{\rm LSDA}(\boldsymbol{r},t;R) + v_{c\sigma}^{\rm LSDA}(\boldsymbol{r},t;R) \\ &\quad - \frac{\beta x_\sigma^2(\boldsymbol{r},t)\rho_\sigma^{\frac{1}{3}}(\boldsymbol{r},t;R)}{1+3\beta x_\sigma(\boldsymbol{r},t)\ln\left\{x_\sigma(\boldsymbol{r},t;R)+[x_\sigma^2(\boldsymbol{r},t;R)+1]^{\frac{1}{2}}\right\}}. \end{aligned} \quad (4)$$

It contains two empirical parameters α and β. In Eq. (4), $v_{x\sigma}^{\rm LSDA}$ and $v_{c\sigma}^{\rm LSDA}$ are the local-spin-density-approximation (LSDA) exchange and correlation potentials, which do *not* have the correct asymptotic behavior. The last term is the gradient correction with $x_\sigma(\boldsymbol{r}) = |\nabla\rho_\sigma(\boldsymbol{r})|/\rho_\sigma(\boldsymbol{r})^{4/3}$, which ensures the proper long-range asymptotic behavior $v_{xc\sigma}^{{\rm LB}\alpha} \rightarrow -1/r$ for $r \rightarrow \infty$.

III. HHG POWER SPECTRUM CALCULATIONS

The numerical solution of the time-dependent equations is detailed in an earlier article [21]. We adopt an energy cutoff of 15 hartree and use $220 \times 40 \times 12$ unequally spaced points on a grid in prolate spheroidal coordinates. The grid is denser at the foci.

It was shown that zero-point vibration of N_2 has little effect on HHG, and therefore we approximate the HHG for the ground vibrational state by that for the equilibrium nuclear geometry [6]. Once the electron density $\rho(\boldsymbol{r},t;R_{\rm eq})$ is obtained, the induced dipole moment and dipole acceleration can be determined, as

$$d(t) = \iiint \rho(\boldsymbol{r},t;R_{\rm eq})q\,d^3\boldsymbol{r}, \quad (5)$$

where $q = \boldsymbol{r}\cdot\hat{\boldsymbol{q}}$ and

$$\begin{aligned} a(t) &= \sum_\sigma \iiint \rho_\sigma(\boldsymbol{r},t;R_{\rm eq}) \\ &\quad \times \left[-\frac{\partial V_{\rm nucl}(\boldsymbol{r};R_{\rm eq})}{\partial q} + E(t)\sin(\omega t)\right]d^3\boldsymbol{r}, \end{aligned} \quad (6)$$

respectively. The HHG power spectrum is related to the Fourier transform of the respective time-dependent dipole moment,

$$d(\omega) = \frac{1}{t_f - t_i}\int_{t_i}^{t_f} d(t)e^{-i\omega t}dt, \tag{7}$$

or dipole acceleration,

$$a(\omega) = \frac{1}{t_f - t_i}\int_{t_i}^{t_f} a(t)e^{-i\omega t}dt = -\omega^2 d(\omega). \tag{8}$$

The spectral density (radiation energy per unit frequency range) is given by [25]

$$S(\omega) = \frac{2}{3\pi c^3}|a(\omega)|^2 = \frac{2\omega^4}{3\pi c^3}|d(\omega)|^2, \tag{9}$$

where c is the speed of light. We have checked that results obtained by calculating a and d are indistinguishable, which is an indication of numerical accuracy. Throughout the paper we plot $|a(\omega)|^2$ as the HHG power spectrum.

To demonstrate the involvement of inner valence electrons and to analyze the occurrence of resonances, we only present HHG calculations for two orientations of the molecular axis: it is either parallel or perpendicular to the laser polarization. We have performed calculations to verify that for other orientations presence of inner valence contributions and resonances are from similar sources as those for the parallel or perpendicular orientations.

IV. HHG AT THE PARALLEL ORIENTATION

Figure 1 shows the calculated HHG spectra for N_2 in 1300 and 800 nm laser fields with intensities of 10^{14} and 2.5×10^{14} W/cm^2, respectively. In both cases there is an enhanced region around 20–35 eV. A monotonic decay occurs beyond 35 eV. A Cooper like minimum is located at 39.0 eV for HHG in the 800 nm laser and at 41.0 eV for HHG in the 1300 nm laser.

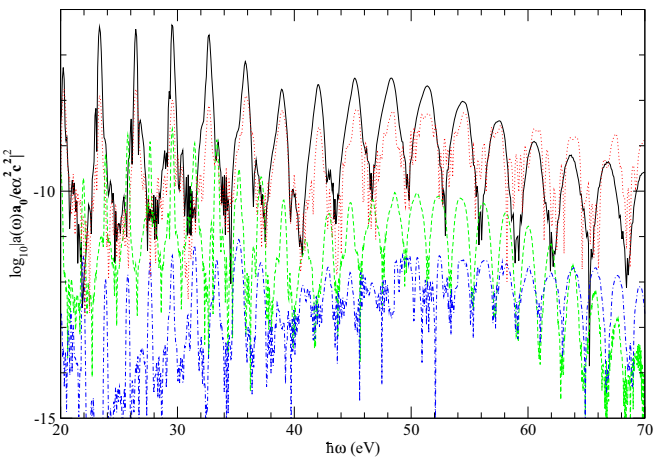

FIG. 1. Calculated HHG spectra of N_2 at the equilibrium internuclear distance in linearly polarized lasers with an intensity of 10^{14} W/cm^2 and a wavelength of 1300 nm at the parallel orientation (green dashed line) and at the perpendicular orientation (blue dashed dotted line), and in lasers of 2.5×10^{14} W/cm^2 with a 800-nm wavelength at the parallel orientation (black solid line) and at the perpendicular orientation (red dotted line). α is the fine-structure constant, and e is the elementary charge.

Consistent with the findings by Jin *et al.* [7], the largest spectral densities are at 29.6 eV for the parallel orientation. For the 800-nm laser, the intensity at 29.6 eV is more than an order of magnitude higher than that for the perpendicular orientation. For the 1300-nm laser it is more than two orders of magnitude higher.

Beyond 60 eV, harmonics decrease more substantially for the parallel orientation and the intensities at the cutoff region are lower than those for the perpendicular orientation.

A. Resonance enhanced emissions at 20–35 eV

The HHG intensities at 20–35 eV are much larger than those at the plateau of 45–55 eV. They are also much larger than those for the perpendicular orientation (Fig. 1). In order to analyze contributions from different orbitals we plot, in Fig. 2,

$$|a_{i\sigma}(\omega)|^2 = \left|\frac{1}{t_f - t_i}\int_{t_i}^{t_f} a_i(t)e^{-i\omega t}dt\right|^2, \tag{10}$$

where

$$a_{i\sigma}(t) = \iiint \rho_{i\sigma}(\boldsymbol{r},t;R_{\rm eq}) \times \left[-\frac{\partial V_{\rm nucl}(\boldsymbol{r};R_{\rm eq})}{\partial q} + E(t)\sin(\omega t)\right]d^3\boldsymbol{r}. \tag{11}$$

Strictly speaking, the contribution of a spin orbital $i\sigma$ is not only $|a_{i\sigma}(\omega)|^2$ but its interference term with other orbitals as well. Nevertheless, $|a_{i\sigma}(\omega)|^2$ provides a good indication of the contribution and the difference $|a(\omega)|^2 - \sum_{i\sigma}|a_{i\sigma}(\omega)|^2$ is the sum of all interference terms. Two intensities are included for each wavelength in Fig. 2 and the largest contribution is from the HOMO for all four sets of laser parameters. Contributions of the HOMO are about an order of magnitude higher than the second largest contribution, those from the HOMO-1.

To confirm that shape resonances, specifically the $3\sigma_g - n\sigma_u$ transitions, play a significant role in the enhancement, we projected $d(R_{\rm eq},\omega)$ to field free dipole matrix elements and separated the contributions from the ion and those from the active electron. Consistent with the earlier analysis [6], the largest contributions for ω between 20 and 35 eV are

$$d_{/\!/}(R_{\rm eq},\omega) = A\langle 3\sigma_u|\hat{z}|\varphi_{\boldsymbol{k}}\rangle + B\langle X\,^2\Sigma_g^+|\hat{z}|C\,^2\Sigma_u^+\rangle + \cdots, \tag{12}$$

where A and B are projection coefficients. Matrix element $\langle 3\sigma_u|\hat{z}|\varphi_{\boldsymbol{k}}\rangle$ describes recombination of the free electron to the $3\sigma_u$ orbital (the LUMO+1). The free electron initially occupies the HOMO. It shows that the $3\sigma_g - 3\sigma_u$ transition is particularly important.

In Eq. (12), the $\langle X\,^2\Sigma_g^+|\hat{z}|C\,^2\Sigma_u^+\rangle$ matrix element is the contribution from the ion, which is dominated by the $1\pi_u - 1\pi_g$ (HOMO-1 $\leftrightarrow$ LUMO) transition. It is consistent with the interpretation that photoionization from the HOMO is enhanced by autoionization that leads to the $C\,^2\Sigma_u^+$ state of N_2^+ [17]. For HHG the photoelectron recombines to the $3\sigma_g$ orbital of the $C\,^2\Sigma_u^+$ state of the ion, and the resulting autoionizing state is in resonance with the $c_4'\,^1\Sigma_u^+$ Rydberg state, which is accessible by recombination of the photoelectron to the $3\sigma_u$ orbital of the ground state of the ion ($X\,^2\Sigma_g^+$).

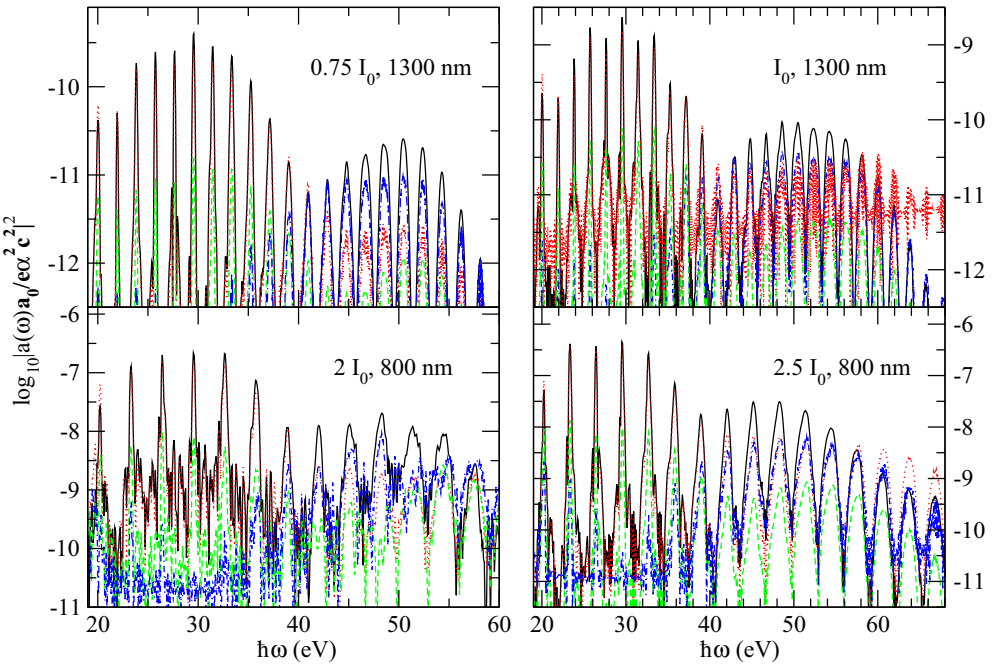

FIG. 2. Contributions of the HOMO (red dotted lines), the HOMO-1 (green dashed lines), and the HOMO-3 (blue dotted dashed lines) to HHG (black solid lines). The polarization direction of the lasers is parallel to the internuclear axis. Laser intensities and wavelengths are labeled in each panel and $I_0 = 10^{14}$ W/cm^2.

B. The minimum near 40 eV and two-center interference

In the earlier study involving a 2×10^{14} W/cm^2 800-nm laser [6], we have shown that inclusion of the symmetry of the $4\sigma_u$ orbital and the ion excitation energy for $X\,^2\Sigma_g^+ \rightarrow C\,^2\Sigma_u^+$ into the two-center interference model (TCIM) leads to the following generalized TCIM (GTCIM) formalism:

$$\hbar\omega_{\min} = \frac{\hbar^2\pi^2}{2m_e R^2} + \Delta E_{\rm exc}^{\rm ion}(R), \tag{13}$$

in which $\omega_{\min}$ is the angular frequency for the minimum, m_e is the electron mass, R is the nuclear separation, and the excitation energy $\Delta E_{\rm exc}^{\rm ion}$ is approximated as the orbital energy difference between $1\pi_g$ and $1\pi_u$.

When minima predicted by the GTCIM formalism and TDDFT calculations agree, it shows that two-center interference diminishes the contributions from the $3\sigma_g \rightarrow 3\sigma_u$ Rydberg state and autoionization state that converges to the $C\,^2\Sigma_u^+$ state of N_2^+. Both $3\sigma_g \rightarrow 3\sigma_u$ and $X\,^2\Sigma_g^+ \rightarrow C\,^2\Sigma_u^+$ involve many photons, and the question arises whether wavelengths and intensities of the incident laser influence resonances, and thus shift the HHG minimum.

In Fig. 3, we plot the HHG spectra for 10^{14} W/cm^2, 1300-nm lasers and 2.5×10^{14} W/cm^2, 800-nm lasers calculated for a set of internuclear distances at the parallel orientation. The minima predicted by the two methods agree. This is an indication that, for a wide range of laser wavelengths and intensities, the reduced intensities near the 40 eV minimum can be assigned to a shape resonance.

C. Contributions of the $2\sigma_g$ orbital

The energy for removing an electron from the $2\sigma_g$ orbital (the HOMO-3) is measured to be 37.3 eV [26]. Figure 2 shows that contributions of the $2\sigma_g$ orbital become significant above 40 eV, regardless of the laser intensity or wavelength.

The energy separation between the $3\sigma_g$ and $2\sigma_g$ orbitals is 21.5 eV. Coupling between the two orbitals via an even number of photons may be possible. This coupling involves an even number of photons due to the selection rule. This coupling requires 11.9 photons for 800-nm lasers and 18.5 photons for 1300-nm lasers. We therefore expect the coupling in 800-nm lasers of higher intensities to be stronger than that in 1300-nm lasers of weaker intensities. As expected, the contribution of the $2\sigma_g$ orbital relative to that of the HOMO depends on the wavelengths of the incident light. In a 2.5×10^{14} W/cm^2, 800-nm laser, contributions of the $3\sigma_g$ and $2\sigma_g$ orbitals are similar between 45 and 55 eV, due to a stronger coupling between the two (Fig. 2). For 7.5×10^{13} W/cm^2, 1300-nm lasers, on the other hand, the contribution of the $2\sigma_g$ orbital is three to four times larger than that of HOMO, which is due to lack of coupling between the two orbitals when the laser intensity is large enough (Fig. 2).

Figure 2 also demonstrates that contributions of the $2\sigma_g$ orbital determine the cutoff intensities. Near the cutoff, the HHG curve overlaps with the $2\sigma_g$ curve. Even though contributions of the HOMO are higher, they interfere destructively with those from the $2\sigma_u$ orbital (HOMO-2) and the two contributions cancel each other.

V. HHG AT THE PERPENDICULAR ORIENTATION

Figure 1 shows that, except for the harmonics near the cutoff, intensities for the perpendicular orientation are lower than those for the parallel orientation. This is consistent with experimental observations [15]. Between 23 and 35 eV, the difference is substantial, which is consistent with predictions

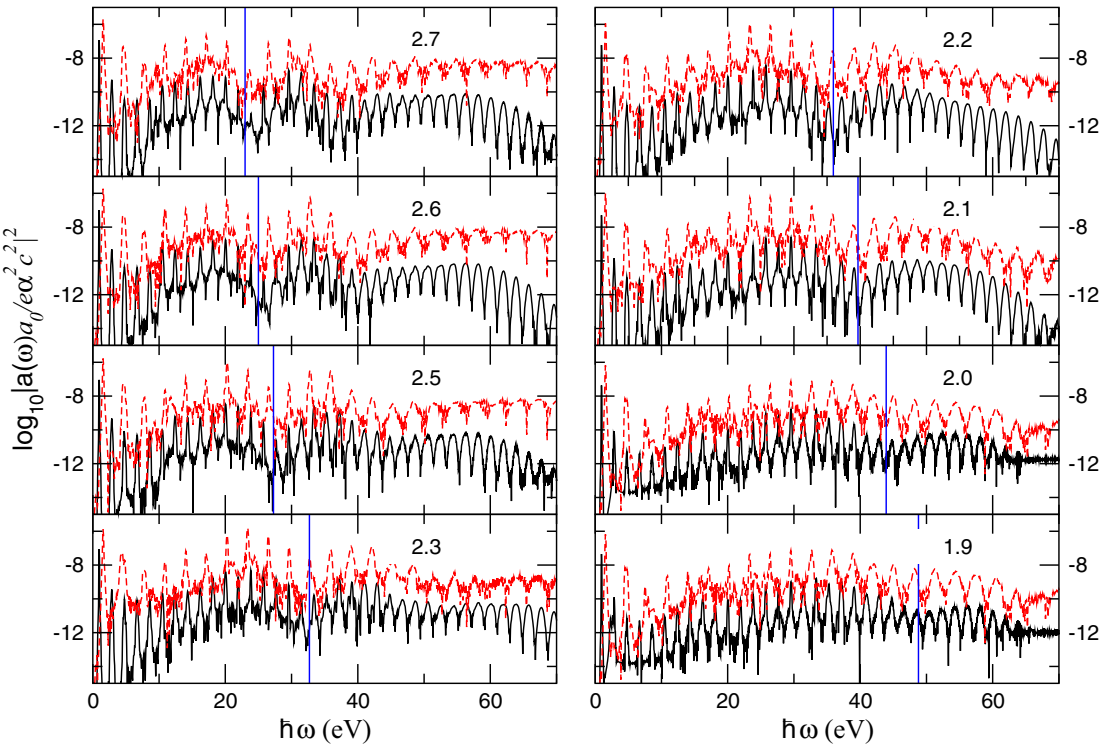

FIG. 3. The HHG of N_2 at a series of internuclear distances for 10^{14} W/cm^2, 1300-nm lasers (black solid lines) and 2.5×10^{14} W/cm^2, 800-nm lasers (red dashed lines). Internuclear distances in units of a_0 are given in each panel. Positions of the Cooper minimum predicted by the generalized two-center interference model that considers shape resonance are given in blue vertical lines. The classical cutoff is 62–63 eV for the 800-nm lasers and 65–66 eV for the 1300-nm lasers. Our method may not accurately resolve peaks beyond the cutoff.

based on QRS calculations [7] and orientation dependent measurements [8]. There is also a minimum near 40 eV. Unlike the one for the parallel orientation, however, the position of the minimum shifts when the laser intensity changes.

A. 20–35 eV

The $3\sigma_g$ HOMO contributes the most in this energy range. Compared to HHG at the parallel orientation, the contribution of the $1\pi_u$ orbital is more substantial. Analysis of the time-dependent solution shows that the major contributors are

$$d_\perp(\omega) = C\langle 2\pi_u|\hat{x}|\varphi_{\boldsymbol{k}}\rangle + D\langle 1\pi_u|\hat{x}|\varphi_{\boldsymbol{k}'}\rangle + E\langle X\,^2\Sigma_g^+|\hat{x}|2\,^2\Pi_u\rangle, \quad (14)$$

where C, D, and E are constants determined by the harmonic order and laser parameters. The first term represents recombination of the active electron, which initially occupies the HOMO, to a $2\pi_u$ Rydberg orbital. The second term is recombination of the photoelectron that initially occupies the HOMO-1. The third term is ion deexcitation.

The sum of the first and third terms constitutes most of the contribution from the HOMO and it is larger than the second term, which is the contribution from the HOMO-1. Recombination of the photoelectron to the $3\sigma_g$ orbital of the $2\,^2\Pi_u$ state of N_2^+ is in resonance with recombination of the photoelectron to the $2\pi_u$ orbital of the ground state of the ion, which enhances the sum of the first and third terms. The $2\,^2\Pi_u$ state arises from the $2\sigma_u \rightarrow 1\pi_g$ transition.

B. Minimum near 40 eV

Similar to the spectra for the parallel orientation, contributions of the HOMO decrease substantially beyond 35 eV, which leads to the minimum near 40 eV. Diminishing of the first and third terms in Eq. (14) reduces the contribution of the HOMO.

The exact energy of the minimum, however, is determined by three factors. First of all, the $C\langle 2\pi_u|\hat{x}|\varphi_{\boldsymbol{k}}\rangle$ term is minimized at a similar energy (or $\boldsymbol{k}$ value) as the $\langle 3\sigma_u|\hat{x}|\varphi_{\boldsymbol{k}}\rangle$ term for the parallel orientation [6]. This is because the nodal structures of the $3\sigma_u$ and $2\pi_u$ orbitals are very similar. Second, the $2\,^2\Pi_u$ state is 3 eV higher than the $C\,^2\Sigma_u^+$ state, which results in a difference between the perpendicular and parallel orientation. Finally, both $1\pi_u$ and $2\sigma_g$ orbitals contribute significantly at 40 eV; therefore, interference between the dipole matrix elements that involve these orbitals and that involve the HOMO play a significant role. Among these factors, the interference involving the HOMO and HOMO-1 was discussed by Jin *et al.* [7].

The laser intensity plays a significant role in multiphoton resonances and hence in the contribution of the HOMO and its interference with other channels. For 1300-nm lasers, the minimum is at 37 eV for an intensity of 7.5×10^{13} W/cm^2 and at 39 eV for 10^{14} W/cm^2 (Fig. 4). For 800-nm lasers, the minimum is at 39 eV for 2×10^{14} W/cm^2 and at 42 eV for an intensity of 2.5×10^{14} W/cm^2.

C. Beyond 40 eV

Near 42 eV, contributions of the $2\sigma_g$ orbital exceed those of the HOMO and become dominant (Fig. 4). The HOMO-1

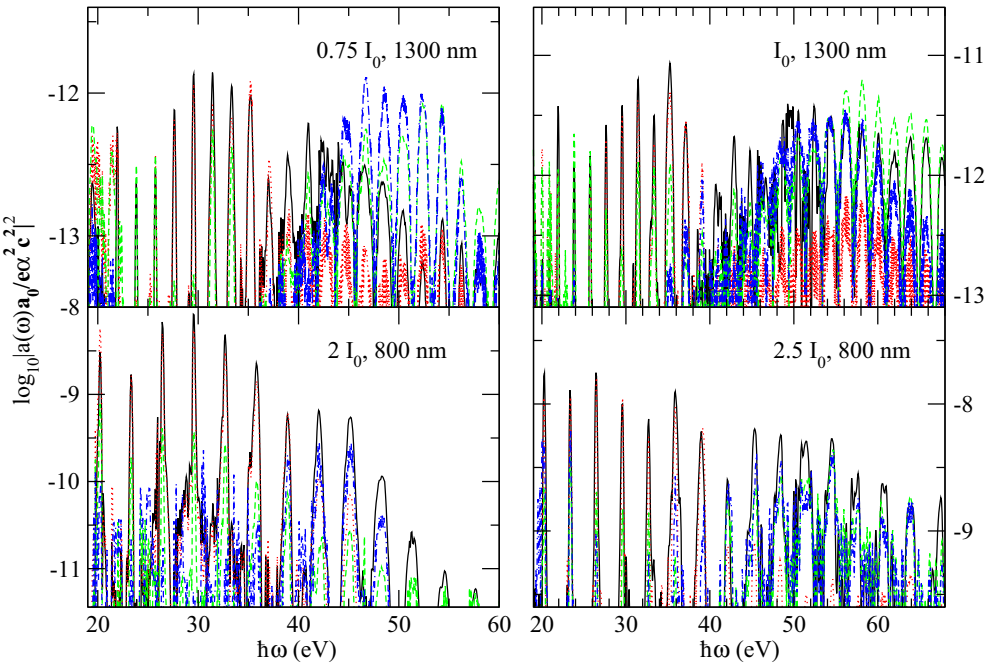

FIG. 4. Contributions of the HOMO (red dotted lines), the HOMO-1 (green dashed lines), and the HOMO-3 (blue dotted dashed lines) to HHG (black solid lines). The polarization direction of the lasers is perpendicular to the internuclear axis. Laser intensities and wavelengths are labeled in each panel and $I_0 = 10^{14}$ W/cm^2.

contributes significantly above 56 eV (Fig. 4). Beyond the cutoff, the most significant contribution is from the HOMO-1, which is consistent with studies by McFarland *et al.* [15]. Our calculations show that, for any molecular orientation relative to the laser field, the $2\sigma_g$ orbital contributes significantly between 42 and 56 eV, as long as HHG in this range is below the cutoff.

For both 800- and 1300-nm lasers of higher intensities in particular, some harmonics between 42 and 56 eV have similar contributions from the $2\sigma_g$ and $1\pi_u$ orbitals. We interpret this as an indication of multiphoton coupling between the two orbitals through an odd number of photons. Their energy difference in our calculation amounts to 17.0 photons for the 1300-nm laser and to 10.4 photons for 800-nm lasers.

VI. SUMMARY AND CONCLUSIONS

Using TDDFT calculations that include all electrons and multiple configurations, we study HHG of N_2. Our calculations have reproduced the following known features of HHG spectra of N_2: a shape resonance, the Cooper minimum, and the higher intensities for the perpendicular orientation compared to the parallel orientation near the cutoff harmonics, which is due to contributions from the HOMO-1 orbital.

For the shape resonance, our analysis shows the importance of multiphoton resonances between Rydberg and autoionizing states, which is ignored in other model studies. We also demonstrate that for the perpendicular orientation, the position of the Cooper minimum is shifted relative to the parallel orientation due to the anisotropy in ion polarization and three channel interference of the photoelectron.

We discover that the inner valence $2\sigma_g$ orbital makes a significant contribution between 42 and 56 eV regardless of the molecular orientation or laser parameters, which, to our best knowledge, has not yet been discussed.

ACKNOWLEDGMENT

This work is supported by the National Science Foundation Award No. PHY-1506441.

[1] J. Itatani, J. Levesque, D. Zeidler, H. Niikura, H. Pépin, J. Kieffer, P. Corkum, and D. Villeneuve, Nature **432**, 867 (2004).

[2] S. Haessler, J. Caillat, W. Boutu, C. Giovanetti-Teixeira, T. Ruchon, T. Auguste, Z. Diveki, P. Breger, A. Maquet, B. Carré *et al.*, Nat. Phys. **6**, 200 (2010).

[3] C. I. Blaga, J. Xu, A. D. DiChiara, E. Sistrunk, K. Zhang, P. Agostini, T. A. Miller, L. F. DiMauro, and C. D. Lin, Nature **483**, 194 (2012).

[4] H. Wörner, J. Bertrand, D. V. Kartashov, P. B. Corkum, and D. M. Villeneuve, Nature **466**, 604 (2010).

[5] J. B. Bertrand, H. J. Wörner, P. Hockett, D. M. Villeneuve, and P. B. Corkum, Phys. Rev. Lett. **109**, 143001 (2012).

[6] X. Chu and G. C. Groenenboom, Phys. Rev. A **87**, 013434 (2013).

[7] C. Jin, J. B. Bertrand, R. R. Lucchese, H. J. Wörner, P. B. Corkum, D. M. Villeneuve, A.-T. Le, and C. D. Lin, Phys. Rev. A **85**, 013405 (2012).

[8] X. Ren, V. Makhija, A.-T. Le, J. Troß, S. Mondal, C. Jin, V. Kumarappan, and C. Trallero-Herrero, Phys. Rev. A **88**, 043421 (2013).
[9] K. J. Schafer, B. Yang, L. F. DiMauro, and K. C. Kulander, Phys. Rev. Lett. **70**, 1599 (1993).
[10] P. B. Corkum, Phys. Rev. Lett. **71**, 1994 (1993).
[11] M. Lewenstein, Ph. Balcou, M. Y. Ivanov, A. L'Huillier, and P. B. Corkum, Phys. Rev. A **49**, 2117 (1994).
[12] L. V. Keldysh, J. Exptl. Theoret. Phys. (U.S.S.R.) **47**, 1945 (1964).
[13] F. H. M. Faisal, J. Phys. B **6**, L89 (1973).
[14] H. R. Reiss, Phys. Rev. A **22**, 1786 (1980).
[15] B. K. McFarland, J. P. Farrell, P. H. Bucksbaum, and M. Gühr, Science **322**, 1232 (2008).
[16] A. Hamnett, W. Stoll, and C. E. Brion, J. Electron. Spectrosc. Relat. Phenom. **8**, 367 (1976).
[17] E. W. Plummer, T. Gustafsson, W. Gudat, and D. E. Eastman, Phys. Rev. A **15**, 2339 (1977).
[18] Y. Huang, C. Meng, X. Wang, Z. Lü, D. Zhang, W. Chen, J. Zhao, J. Yuan, and Z. Zhao, Phys. Rev. Lett. **115**, 123002 (2015).
[19] X. Chu, Phys. Rev. A **82**, 023407 (2010).
[20] X. Chu and G. C. Groenenboom, Phys. Rev. A **85**, 053402 (2012).
[21] X. Chu and M. McIntyre, Phys. Rev. A **83**, 013409 (2011).
[22] X. Chu and Shih-I Chu, Phys. Rev. A **63**, 023411 (2001).
[23] X. Chu and Shih-I Chu, Phys. Rev. A **64**, 063404 (2001).
[24] X. Chu and P. J. Memoli, Chem. Phys. **391**, 83 (2011).
[25] D. A. Telnov and Shih-I Chu, Phys. Rev. A **80**, 043412 (2009).
[26] A. Lofthus and P. H. Krupenie, J. Phys. Chem. Ref. Data **6**, 113 (1977).